



Originally published as:

Drozdo, A. Y., Shprits, Y., Usanova, M. E., Aseev, N., Kellerman, A. C., Zhu, H. (2017): EMIC wave parameterization in the long-term VERB code simulation. - *Journal of Geophysical Research*, 122, 8, pp. 8488—8501.

DOI: <http://doi.org/10.1002/2017JA024389>

## RESEARCH ARTICLE

10.1002/2017JA024389

## Key Points:

- Addition of EMIC waves improves the long-term simulation of multi-MeV electron dynamics
- Solar wind dynamic pressure provides better parameterization of EMIC wave presence than  $K_p$ ,  $Dst$ , and  $AE$  indices and solar wind velocity
- Simulation with parameterized EMIC waves reproduces a phase space density deepening minimum

## Supporting Information:

- Supporting Information S1

## Correspondence to:

A. Y. Drozdov,  
adrozdov@ucla.edu

## Citation:

Drozdov, A. Y., Y. Y. Shprits, M. E. Usanova, N. A. Aseev, A. C. Kellerman, and H. Zhu (2017), EMIC wave parameterization in the long-term VERB code simulation, *J. Geophys. Res. Space Physics*, 122, 8488–8501, doi:10.1002/2017JA024389.


Received 25 MAY 2017

Accepted 1 AUG 2017

Accepted article online 7 AUG 2017

Published online 24 AUG 2017

## EMIC wave parameterization in the long-term VERB code simulation

A. Y. Drozdov<sup>1</sup> , Y. Y. Shprits<sup>2,3,1</sup> , M. E. Usanova<sup>4</sup> , N. A. Aseev<sup>2,3</sup> , A. C. Kellerman<sup>1</sup> , and H. Zhu<sup>5</sup> 

<sup>1</sup>Department of Earth, Planetary and Space Sciences, University of California, Los Angeles California, USA, <sup>2</sup>Helmholtz Centre Potsdam, GFZ German Research Centre for Geosciences, Potsdam, Germany, <sup>3</sup>Institute for Physics and Astronomy, University of Potsdam, Potsdam, Germany, <sup>4</sup>Laboratory for Atmospheric and Space Physics, University of Colorado Boulder, Boulder, Colorado, USA, <sup>5</sup>William B. Hanson Center for Space Sciences, Department of Physics, University of Texas at Dallas, Richardson, Texas, USA

**Abstract** Electromagnetic ion cyclotron (EMIC) waves play an important role in the dynamics of ultrarelativistic electron population in the radiation belts. However, as EMIC waves are very sporadic, developing a parameterization of such wave properties is a challenging task. Currently, there are no dynamic, activity-dependent models of EMIC waves that can be used in the long-term (several months) simulations, which makes the quantitative modeling of the radiation belt dynamics incomplete. In this study, we investigate  $K_p$ ,  $Dst$ , and  $AE$  indices, solar wind speed, and dynamic pressure as possible parameters of EMIC wave presence. The EMIC waves are included in the long-term simulations (1 year, including different geomagnetic activity) performed with the Versatile Electron Radiation Belt code, and we compare results of the simulation with the Van Allen Probes observations. The comparison shows that modeling with EMIC waves, parameterized by solar wind dynamic pressure, provides a better agreement with the observations among considered parameterizations. The simulation with EMIC waves improves the dynamics of ultrarelativistic fluxes and reproduces the formation of the local minimum in the phase space density profiles.

### 1. Introduction

Earth's outer radiation belt includes a highly variable population of trapped relativistic ( $\sim 1$  MeV) and ultrarelativistic ( $> 3$  MeV) electrons. Major variations in electron fluxes generally happen during geomagnetic storms and may exceed several orders of magnitude [Reeves *et al.*, 2003]. The electrons of such high energies can damage spacecraft instrumentation [Baker *et al.*, 1987]. However, despite the importance of space infrastructure, accurate modeling of flux variability at both relativistic and ultrarelativistic energies still remains a challenging task [e.g., Drozdov *et al.*, 2015].

Previous studies discussed that the dynamics of ultrarelativistic electrons can be different from the relativistic population. For instance, Baker *et al.* [2013a] showed that a very narrow, unexpected third belt consisting of ultrarelativistic electrons can be formed and can exist for over a month. Shprits *et al.* [2013] suggested that various physical processes determines the evolution of ultrarelativistic electrons, and additional scattering due to electromagnetic ion cyclotron (EMIC) wave-particle interaction is required to explain the formation of the third belt. Evidence that an additional loss mechanism is necessary to explain the ultrarelativistic electrons dynamics was also discussed by Drozdov *et al.* [2015]. The authors showed that their model fluxes of ultrarelativistic electrons were significantly larger than the observed values; the corresponding decay rates significantly overestimated the observations when, for the relativistic electrons, decay rates were in agreement with the measurements. Recently, Shprits *et al.* [2016] included EMIC waves into a numerical simulation of the outer radiation belt fluxes and reproduced the different observed dynamics of relativistic and ultrarelativistic electrons during the January 2013 magnetic storm.

Theory showed that EMIC waves are very effective at multi-MeV electron scattering and may play an important role in ultrarelativistic electron dynamics [Lyons and Thorne, 1972; Summers and Thorne, 2003; Ukhorskiy *et al.*, 2010]. EMIC wave scattering is fast at low pitch angles and significantly slower at high pitch angles, causing a narrowing in electron pitch angle distribution, more pronounced at high energies [Usanova *et al.*, 2014]. Acting as a rapid local loss process, EMIC waves can produce a deepening local minimum of phase space density (PSD) [Shprits *et al.*, 2017]. At the same time, the lower energy electrons ( $\leq 1$  MeV) are generally unaffected by EMIC waves [Horne and Thorne, 1998; Meredith *et al.*, 2003].

In contrast to event-specific simulations, a long-term simulation (several months) includes many different geomagnetic events covering various cases of the radiation belts dynamics. Different processes in the long-term simulation can be described using statistical models of wave and plasma properties. In particular, the global radial and local pitch angle and energy diffusion is described by diffusion coefficients derived from statistical observations of various plasma wave modes (e.g., ULF and whistler) under different geomagnetic conditions. Previous studies using this simulation approach [Subbotin *et al.*, 2011; Kim and Shprits, 2013] showed a reasonably good agreement between the model relativistic electron fluxes and observations. However, EMIC waves were not included in those simulations, because they are often quite localized and transient [Blum *et al.*, 2016], which makes EMIC waves difficult to include in long-term modeling. Without additional loss source of ultrarelativistic electrons, the model flux overestimated the observations [Drozdov *et al.*, 2015]. Hence, the parameterization of EMIC wave presence is necessary for accurate modeling of radiation belts.

Quasi-linear simulations with parameterized EMIC waves have been performed before. Kersten *et al.* [2014] presented a long-term simulation of ultrarelativistic electron fluxes with EMIC waves parameterized by  $Kp$  index. The parameterization was based on statistical wave parameters obtained from the Combined Release and Radiation Effects Satellite (CRRES) measurements. However, the results of the simulation were not compared with observations. Ma *et al.* [2015] simulated the ultrarelativistic electron flux decay during the 10 day interval from 6 to 16 March 2013 and used amplitude and spectral characteristics of EMIC waves from Meredith *et al.* [2014]. EMIC wave activity was parameterized by the  $Kp$  index and included in the simulation only when  $Kp \geq 2$  (~16% of the time) at  $L^* \geq 4$  ( $L^*$  is the generalized  $L$  value [Roederer, 1970]). However, Thorne *et al.* [2013a] reproduced the decay of ultrarelativistic electron fluxes during another period from 7 to 19 September 2012, using only scattering by hiss waves, despite the fact that  $Kp$  index during this period was larger than or equal to 2, even more often (~27% of the time). However, Usanova *et al.* [2012] showed that  $Kp$  index is not a good predictor for EMIC wave occurrence. Hence, the  $Kp$  index may not accurately describe the presence of EMIC waves. In addition, Ma *et al.* [2015] used a relatively small constant EMIC intensity of  $0.1 \text{ nT}^2$  in their simulation. However, larger amplitude ( $B_w$ ), ~1 nT waves are commonly observed [e.g., Fraser and Nguyen, 2001; Usanova *et al.*, 2008; Ukhorskiy *et al.*, 2010; Meredith *et al.*, 2014] and even larger [Engebretson *et al.*, 2015]. In this paper, we investigate EMIC waves of various  $B_w$  in the long-term simulations.

Besides the  $Kp$  index, the EMIC wave activity can be parametrized by other geomagnetic indexes or other drivers of magnetospheric dynamics. Several papers focused on the relationship between EMIC wave observations and the  $AE$  index,  $SYM-H$  (or  $Dst$  index), and solar wind parameters [e.g., Usanova *et al.*, 2008, 2012; Halford *et al.*, 2010, 2016; Tetrick *et al.*, 2017]. The authors found a correlation between considered parameters; however, the question of which parameter determines the presence of the EMIC waves is still open.

In this study, we perform multiple long-term simulations using various parameterizations of EMIC wave presence using  $Kp$ ,  $Dst$ , and  $AE$  indices, solar wind speed, and dynamic pressure. In addition, for each parameterization, we perform several runs with various EMIC waves at  $B_w$ . A selection of the best parameterization is based on the comparison of the simulation results and observations. To find this, we calculate the mean absolute error between simulation and observations accompanied by a direct comparison of the model and observed electron fluxes, pitch angle distributions, and phase space densities.

## 2. Observations

### 2.1. Van Allen Probes

The Van Allen Probes [Mauk *et al.*, 2013] mission was launched on 30 August 2012, to study the dynamical evolution of the radiation belts. The spacecraft are equipped with identical sets of instruments designed for monitoring the radiation belt particle and wave environment. Particles with energies ranging from hot to ultrarelativistic are measured using the Energetic particle, Composition, and Thermal plasma (ECT) suite, which includes Magnetic Electron Ion Spectrometer (MagEIS) and Relativistic Electron Proton Telescope (REPT) instruments [Baker *et al.*, 2013b; Blake *et al.*, 2013; Funsten *et al.*, 2013].

In the current study, we use measurements of electrons in the energy range from ~30 keV to ~4 MeV from the MagEIS instrument and from 1.8 MeV to 10s of MeV from the REPT instrument. Based on pitch angle resolved flux measurements, PSD is calculated for a wide spatial range of  $L^*$  from ~1 to 5.5 using the TS07D magnetic field model [Tsyganenko and Sitnov, 2007].

### 3. Methodology

#### 3.1. The VERB Code

The evolution of electron distribution function or phase space density (PSD) can be described using the Fokker-Planck equation [Schulz and Lanzerotti, 1974]. Wave-particle interactions may violate all three adiabatic invariants and can result in radial transport, local acceleration, or loss of electrons. The 3-D Fokker-Planck equation takes into account described processes. In particular, it includes radial diffusion caused by ultralow frequency (ULF) waves, pitch angle, energy, and mixed diffusion caused by whistler and EMIC waves and particle losses in the atmosphere or at the magnetopause boundary.

The Versatile Electron Radiation Belt (VERB) code [Subbotin and Shprits, 2009] is designed to model the radiation belt dynamics by solving the Fokker-Planck equation numerically. Subbotin and Shprits [2009] solved the 3-D Fokker-Planck equation by separating it into the radial and local diffusion operators on two grids. Both operators were written in terms of  $L^*$ , where radial diffusion simulations were conducted on a grid of constant adiabatic invariants, while pitch angle and energy simulations were performed on a grid which is orthogonal in pitch angle and energy. Most of the 3-D diffusion codes [e.g., Su et al., 2011; Tu et al., 2013; Glauert et al., 2014] used this approach. However, Subbotin and Shprits [2012] suggested the improvement of 3-D simulations using a single grid of modified adiabatic invariants. This approach was included into the VERB code and allowed to exclude the interpolation between the numerical grids since the interpolation can either lead to numerical errors or unstable behavior of the code.

In this formulation, the Fokker-Planck equation on the single grid can be written as

$$\begin{aligned} \frac{\partial f}{\partial t} = & \frac{1}{G} \frac{\partial}{\partial L^*} \Big|_{V,K} G \langle D_{L^*L^*} \rangle \frac{\partial f}{\partial L^*} \Big|_{V,K} + \frac{1}{G} \frac{\partial}{\partial V} \Big|_{L^*,K} G \left( \langle D_{VV} \rangle \frac{\partial f}{\partial V} \Big|_{L^*,K} + \langle D_{VK} \rangle \frac{\partial f}{\partial K} \Big|_{L^*,K} \right) \\ & + \frac{1}{G} \frac{\partial}{\partial K} \Big|_{L^*,V} G \left( \langle D_{KK} \rangle \frac{\partial f}{\partial K} \Big|_{L^*,V} + \langle D_{VK} \rangle \frac{\partial f}{\partial V} \Big|_{L^*,V} \right) - \frac{f}{\tau} \end{aligned} \quad (1)$$

where  $f$  is the three-dimensional PSD;  $V$  and  $K$  are the modified adiabatic invariants,  $V \equiv \mu \cdot (K + 0.5)^2$ ,  $K \equiv J / \sqrt{8m_0\mu}$ ;  $\mu$  is first adiabatic invariant;  $m_0$  is the electron mass;  $\langle D_{L^*L^*} \rangle$  is radial diffusion coefficients;  $\langle D_{VV} \rangle$ ,  $\langle D_{KK} \rangle$ , and  $\langle D_{VK} \rangle$  are the bounce-averaged diffusion coefficients;  $G = -2\pi B_0 R_E^2 L^{*-2} \sqrt{8\mu m_0} / (K + 0.5)^2$  is the Jacobian of the transformation from an adiabatic invariant system  $(\mu, J, \Phi)$ ;  $R_E$  is the Earth's radius;  $B_0 = 0.3$  G is the field on the equator at the Earth's surface,  $c$  is the speed of light; and  $f/\tau$  is the loss term, where  $\tau$  represents the electron's lifetime inside the loss cone and is equal to a quarter of the bounce period.  $V$  and  $K$  are convenient for numerical calculations and definition of the boundary conditions because  $K$  is independent of the particle's energy, and  $V$  is weakly dependent on the particle's pitch angle.

#### 3.2. Diffusion Coefficients

The  $Kp$ -dependent radial diffusion coefficient adopted from Brautigam and Albert [2000] was previously used in VERB code long-term simulations (100–200 days) [e.g., Subbotin et al., 2011; Kim and Shprits, 2013], and the model results agreed well with the observations of relativistic electron fluxes. Drozdov et al. [2017] showed that using newer radial diffusion parameterization by Ozeke et al. [2014] does not significantly change the results of the long-term (1 year) VERB simulations which are more sensitive to the local processes, such as wave-particle interactions with whistler mode waves. Consistent with previous studies, we use radial diffusion coefficients from Brautigam and Albert [2000].

The simulation takes into account dayside and nightside chorus waves that produce diffusion outside the plasmasphere. Inside the plasmasphere, the simulations include hiss waves, lightning-generated whistler waves, and anthropogenically generated very low frequency (VLF) waves. The bounce-averaged diffusion coefficients for those waves are computed using the Full Diffusion Code [Shprits and Ni, 2009]. The chorus and the hiss wave frequency and amplitude statistical model is obtained based on the Van Allen Probes measurements [Spasojevic et al., 2015; M. Spasojevic, personal communication, 2016]. The wave spectrum and wave normal angle distributions are defined by Gaussian function. The wave intensity is defined as a function of  $Kp$  index. Wave frequency, intensity, and wave normal angle distribution for VLF plasma waves and lightning-generated whistlers are taken from Subbotin et al. [2011]. The location of the plasmapause is calculated following Carpenter and Anderson [1992].

**Table 1.** Threshold Values of the Simulation Parameters

Parameter	Range	Step	Number of Runs for each $B_w^2$
$Kp$	[0 6]	1	7
$Dst$ (nT)	[-100 0]	10	11
$V_{sw}$ (km/s)	[250 580]	30	12
$P_{dyn}$ (nPa)	[0 10]	1	11
$AE$ (nT)	[0 1200]	100	13

The diffusion coefficients for helium band EMIC waves are calculated with the spectral properties from Meredith *et al.* [2014], similar to those in Ma *et al.* [2015] at a fixed  $B_w^2$  of 0.1 nT<sup>2</sup>. The spectrum is approximated by Gaussian function. A central frequency, frequency bandwidth, and lower and upper cutoff frequencies are  $3.6 f_{O+}$ ,  $0.25 f_{O+}$ ,  $3.35 f_{O+}$ , and  $3.85 f_{O+}$ , where  $f_{O+}$  is oxygen gyrofrequency. The coefficients are scaled according to these waves' magnetic local time (MLT) distribution (25%) and wave occurrence rate (2%) following Meredith *et al.* [2014]. It should be noted that  $B_w^2$ , MLT distribution, and wave occurrence rate are linear multipliers in the EMIC wave diffusion coefficients. The contribution for each of those three factors is independent and results in a single multiplier of the diffusion coefficients. Summers and Thorne [2003] showed that multi-ion (H+, He+, and O+) plasma plays an important role in EMIC wave dispersion relation and affects the electron minimum resonant energy. In this study, the ion composition used in the diffusion coefficient computation is assumed to be 70% H+, 20% He+, and 10% O+ following Meredith *et al.* [2003].

### 3.3. Simulations

We performed a number of long-term simulations with and without EMIC waves covering the period from 1 October 2012 to 1 October 2013. This period is chosen to follow up on previous studies by Drozdov *et al.* [2015] and it includes quiet, moderate, and strong geomagnetic activity.

The computational orthogonal grid has  $101 \times 100 \times 46$  points for  $V$ ,  $K$ , and  $L^*$ , respectively. The  $L^*$  range varies from 1.0 to 5.5. The boundary conditions are set at  $L^* = 5.5$  for energies from 10 keV to 10 MeV and pitch angles from 0.7° to 89.3°, respectively. The  $V$  grid points are distributed logarithmically, and the  $K$  and  $L^*$  grid points are distributed linearly.

The initial conditions are obtained from the Van Allen Probes observations. The PSD for the lower  $V$  boundary (10 keV at  $L^* = 5.5$  and adiabatically increases at lower  $L$  shells) is set to an initial value and remains constant, representing the balance between convective losses and sources. The PSD of upper  $V$  boundary corresponds to 10 MeV at  $L^* = 5.5$  and adiabatically increases in energy toward lower  $L$  shells, and its value is set to zero, representing the absence of very high-energy electrons. Lower  $K$  boundary represents the loss cone, and PSD is set to zero. The upper  $K$  boundary condition is set to a zero-gradient PSD, representing the flat distribution at 90° [Horne *et al.*, 2003]. PSD at the lower radial boundary ( $L^* = 1$ ) is set to zero and represents losses into the atmosphere. The PSD required for the upper radial boundary ( $L^* = 5.5$ ) condition is updated at every step of the simulation and obtained from the Van Allen Probes observation. The location of the magnetopause is calculated following Shue *et al.* [1998]. The corresponding  $L^*$  is calculated using the T89 magnetic field model [Tsyganenko, 1989]. However, it never crosses the simulation domain and is not included in the simulations.

### 3.4. EMIC Wave Parameterization

In this study, we considered five parameters that can possibly define the EMIC wave presence in the simulation: the  $Kp$  index ( $Kp$ ),  $Dst$  index ( $Dst$ ), solar wind speed ( $V_{sw}$ ), solar wind dynamic pressure ( $P_{dyn}$ ), and  $AE$  index ( $AE$ ). EMIC waves are included into the simulation only if the certain parameter is larger (or smaller in case of  $Dst$ ) than the threshold value (see Table 1). Every parameter is considered individually, and for each parameter, the number of independent long-term simulations are performed. For every parameter threshold value, there are six independent simulations performed with different  $B_w^2$  of EMIC waves: 0.1 nT<sup>2</sup>, 0.2 nT<sup>2</sup>, 0.3 nT<sup>2</sup>, 0.4 nT<sup>2</sup>, 0.7 nT<sup>2</sup>, and 1.0 nT<sup>2</sup>. Hence, the individual simulation defines the EMIC wave presence by the parameter's threshold value, which includes the EMIC wave of the specific intensity. In total, we performed 325 long-term simulations.

Fraser and Nguyen [2001] investigated the relation between the location of the EMIC waves and location of the plasmopause. Following their findings, we include the diffusion coefficients of EMIC waves into the simulations in the range of  $-1 < \Delta L < 4$ , where  $\Delta L$  is the difference between the location of EMIC waves and the

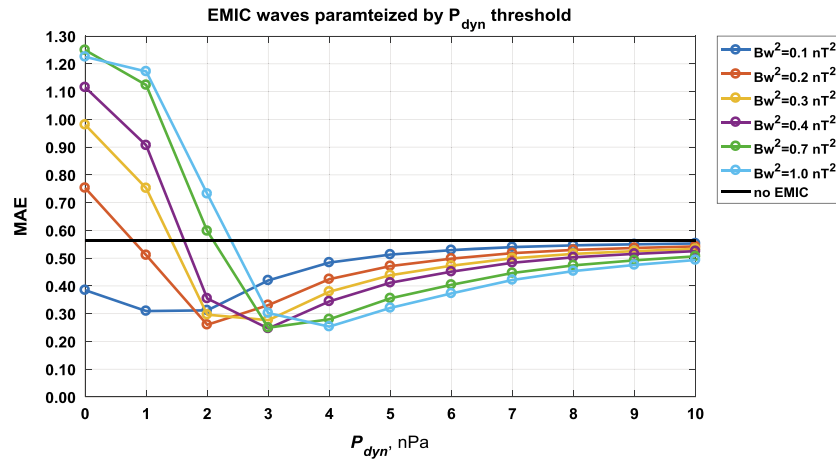


**Figure 1.** MAE from different simulations. Simulations performed with threshold value of solar wind dynamic pressure for various EMIC wave  $B_w^2$ . The colored lines represent different EMIC wave  $B_w^2$ . The black line shows the simulation without EMIC waves.

location of the plasmopause. The EMIC diffusion coefficients outside of this range are set to zero. The location of the plasmopause is calculated following *Carpenter and Anderson [1992]*.

### 3.5. Mean Absolute Error

The determination of the model accuracy for multiple simulations based on different parameters is a difficult task. To narrow the search of optimal parameters from Table 1, its threshold and EMIC wave  $B_w^2$ , which can provide better agreement between the measurement and the simulation, we calculate the mean absolute error (MAE) following *[Kim et al., 2012]*:

$$MAE = \sum_{t, \alpha} \sum_{L^*=2.8}^{L^*=5.5} \left| \frac{\log_{10} J_{obs} - \log_{10} J_{VERB}}{\log_{10} J_{obs}} \right| \Bigg|_{E=4.2 \text{ MeV}} \text{ number of points} \quad (2)$$

where  $t$  is time,  $\alpha$  is pitch angle,  $J_{obs}$  is the differential electron flux of 4.2 MeV electrons, and  $J_{VERB}$  is a the same flux obtained from the VERB long-term simulation. For the MAE calculation,  $J_{obs}$  from both Van Allen Probes spacecraft are binned on the simulation grid cells. The  $J_{obs}$  data points in each cell are averaged and then extrapolated to fill the whole grid. To exclude division on zero, the flux units are converted to  $s^{-1} \text{ sm}^{-2} \text{ sr}^{-1} \text{ MeV}^{-1}$ . In this case, for the selected period, the logarithm of the measured flux is always positive. In comparison to the logarithmic difference, MAE is not biased to the numerically small values of the simulated PSD. MAE excludes the variation of the fluxes in the slot region where the measured flux level is generally comparable with the background noise, and it is focused on the ultrarelativistic population that was not previously reproduced in the long-term simulations *[Drozdov et al., 2015]*.

It is expected that the simulation with a certain combination of EMIC wave parameterization provides lower MAE in comparison to the simulation without EMIC waves. This metric provides a preliminary selection of the parameterizations; however, a detailed analysis of electron fluxes, PSD, and pitch angle distributions is necessary.

## 4. Results

From each individual long-term simulation, we calculate MAE. To find which simulations provide better agreement with the observations, we construct the dependence of MAE on the threshold values of each parameter from Table 1. Figure 1 shows an example of MAE dependence on threshold values of the solar wind pressure, where each point represents an individual long-term simulation, and each color line represents EMIC waves of different  $B_w^2$ . The black line represents MAE for the simulation without EMIC waves. MAE of several simulations is lower in comparison to the simulations without EMIC waves. For most of the selected EMIC waves  $B_w^2$ , the MAE decreases to the minimum with the increase of the solar wind pressure threshold value and then asymptotically approaches the value of the simulation without EMIC waves. The high threshold values represent a near absence of EMIC waves in the simulation since the solar wind

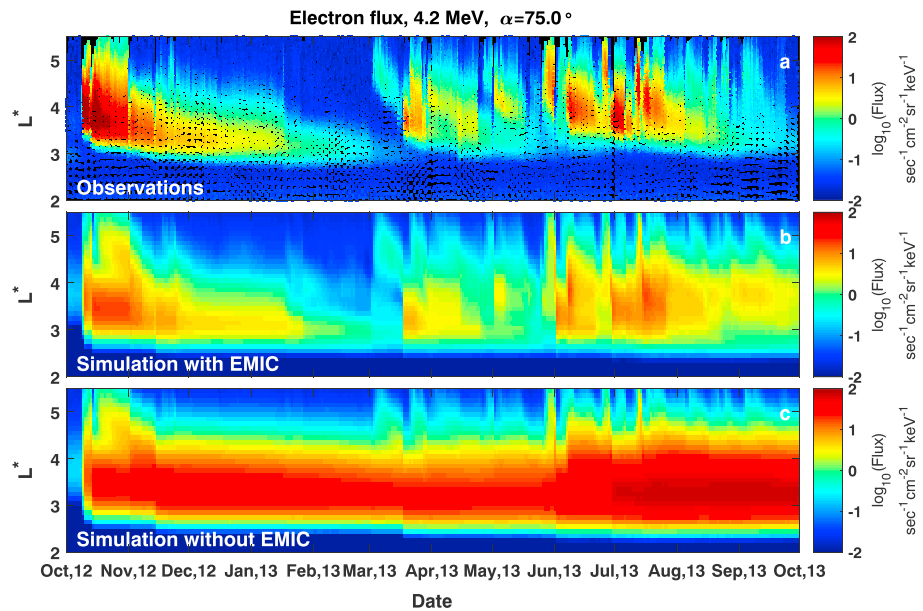


**Figure 2.** Evolution of the 4.2 MeV electron fluxes at equatorial pitch angle ( $\alpha$ ) of  $75^\circ$  as a function of time and  $L^*$ . (a) Detailed REPT observations,  $\alpha = 75^\circ \pm 5^\circ$ , each point represents the 5 min average of the measurements. The black color corresponds to the absence of the measurements. At low  $L^*$ , the satellite moves fast and covers the distance (in  $L^*$ ) that is larger than the size of the time-averaged point which separates them. (b) VERB code simulation results with solar wind pressure parameterized EMIC waves; 0.4 nT<sup>2</sup> EMIC waves are included when  $P_{\text{dyn}} \geq 3$  nPa. (c) VERB code simulation results without EMIC waves.

pressure rarely reaches these values. At the same time, the lower threshold values represent almost constant presence of the EMIC waves in the simulation. Hence, the threshold values at which MAE is minimal represents the possibly optimal presence of the EMIC waves in the simulation. Similar figures for other considered parameters of EMIC wave presence are presented in Figure A1.

There are similar points on Figure 1 that represent low similar MAE for different EMIC wave  $B_w^2$ . This can be explained due to the increase of scattering efficiency with EMIC wave intensity. As discussed in section 1, the modeled ultrarelativistic electron fluxes without EMIC waves are significantly larger than the observed values. Therefore, the increase in the amount of EMIC waves or the increase in their scattering efficiency leads to a decrease in electron flux. Under certain conditions, the combination of the amount of EMIC waves and their scattering efficiency provides a similar ultrarelativistic flux level that is close to the observations (see supporting information Figure S4). We investigate these cases of similar MAE in detail.

As discussed above, we consider several parameters of the EMIC wave presence. Several simulations show similar low MAE. For each of those simulations, we compare the evolution of the electron fluxes (see supporting information Figures S1–S5) and the pitch angle distribution (see supporting information Figures S6–S10) with the observations and the simulation without EMIC waves. We find that the best parameterization is achieved in the case of the solar wind dynamic pressure parameterization with the threshold values of 3 nPa and the wave  $B_w^2$  of 0.4 nT<sup>2</sup> (see Appendix A for details). The detailed analysis of this parameterization is discussed below.

Figure 2 shows the evolution of the ultrarelativistic radiation belt electron fluxes. The simulation with EMIC waves provides a good agreement with the measurements, when the simulation without EMIC waves significantly overestimates the observed fluxes. The relativistic electron fluxes obtained from the same simulations with and without EMIC waves also agreed well with the measurements (see supporting information Figure S11), which is consistent with previous studies [e.g., Kim *et al.*, 2011; Subbotin *et al.*, 2011; Drozdov *et al.*, 2015].

To show that EMIC waves introduce the necessary loss mechanism of ultrarelativistic electrons, we present flux line plots in Figure 3 for three different  $L^*$  values. The flux variation that is modeled with the EMIC wave agrees well with the observation, while the simulation without EMIC waves differs from the measurements. For a quantitative comparison and for the loss mechanism validation, similar to Drozdov *et al.* [2015], we calculate the empirical decay times for the period from 21 November 2012 to 10 January 2013, following

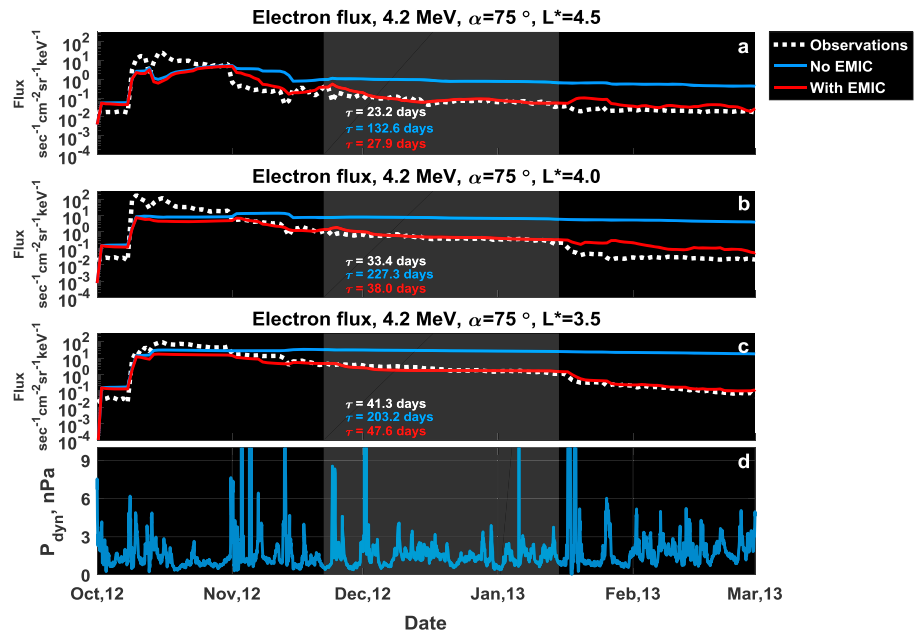


**Figure 3.** The electron flux evolution of 4.2 MeV electron fluxes at fixed  $L^*$  at the pitch angle of  $75^\circ$ . (a)  $L^* = 4.5$ , (b)  $L^* = 4.0$ , and (c)  $L^* = 3.5$ . White dashed line shows observations, blue line shows simulation without EMIC waves, and red line shows simulation with EMIC waves parameterized by solar wind pressure. (d) Solar wind pressure. The highlighted area shows the time period of the empirical decay times ( $\tau$ ) calculation.

the approach described by *Shprits et al.* [2006]. This approach assumes exponential decay; hence for the decay times calculation, it is important to have an approximately linear decrease of the electron flux logarithm value. However, in our case, the period should be long enough to cover the effect from EMIC waves in combination with other loss processes. The selected period covers the times when  $P_{\text{dyn}}$  is larger than 3 nPa (Figure 3d), which triggers EMIC waves in the simulations. Table 2 shows the observed and modeled decay times at various  $L^*$ . The simulation with EMIC waves provides decay times that are very close to the observation, while the decay times from the simulation without EMIC waves are overestimated by a factor of 5–7. These results confirm the conclusion of previous studies and indicate that EMIC waves provide the necessary additional scattering mechanism.

The observations show that relativistic electron fluxes during the 8 October 2012 storm are larger than the modeled flux values, which can be a result of the overestimated modeled losses. This event was discussed by *Thorne et al.* [2013b], and the authors showed that unique low plasma density conditions led to the very efficient local acceleration. The simulations in this study include statistical diffusion coefficients, which are based on the average plasma density. The electron fluxes are similar in both simulations: with and without EMIC waves. Hence, the underestimated flux may result from insufficient local acceleration.

It should be noted that the empirical decay time is a very sensitive parameter for the selected period. To confirm that EMIC waves provide necessary loss process, we use the technique proposed by *Shprits et al.* [2017]. Figure 4 shows the comparison of the evolution of the PSD in inverted colors: the red color represents low PSD values; the blue color represents large PSD values. Figure 4a clearly shows that the PSD local minimum was formed on 17 January 2013 and was observed until 17 March 2013. This period overlaps with the long-term simulation period in Figures 4b and 4c. The simulation with EMIC waves reproduces the PSD formation of the local minimum remarkably, as well as its displacement inward on 1 March 2013, while the simulation without EMIC waves does not show such dynamics. This analysis indicates that included EMIC waves provide the additional loss mechanism at ultrarelativistic energies.

This analysis is not complete without a discussion of the pitch angle distributions. Figure 5 shows the pronounced electron flux rapid decrease during two time periods: from 8 October to 25 November 2012 and from 7 June to 25 July 2013 at fixed  $L^* = 4.5$ . The simulation with EMIC waves shows the pronounced electron flux rapid decrease, simultaneous with the observations. In addition, the observed pitch angle distribution



**Table 2.** The Empirical Decay Times Obtained From Measurement and Simulation of 4.2 MeV Electrons at the Pitch Angle of 75° for Different  $L^*$

$L^*$	Observations (Days)	Simulation With EMIC Waves (Days)	Simulation Without EMIC Waves (Days)
4.5	23.2	27.9	132.6
4.0	33.4	38.0	227.3
3.5	41.3	47.6	203.2

becomes narrower several times, which is a signature of EMIC wave scattering. The simulation shows similar narrowing at multiple times, consistent with the observations. The difference between the simulations and observations can be explained by the use of static parameters of modeled EMIC wave diffusion coefficients. The diffusion coefficients are calculated, assuming the fixed statistical spectrum properties. However, once the EMIC wave spectrum approaches the helium gyrofrequency, the minimum resonant energy decreases, which may lead to more effective scattering due to scattering of the larger pitch angles [e.g., Li et al., 2007]. Further improvement of the simulation requires the time-dependent EMIC wave spectrum for wave diffusion coefficient calculations and will be investigated in the future. In addition, other waves may contribute to the scattering of the equatorial particles such as hiss in the plasmaspheric plume. These waves are not included into the simulations due to the absence of the robust plasmaspheric plume statistical model that can be used in the long-term simulation.

Figure 5 also shows the insufficient modeled electron acceleration at the beginning of both periods. Since both simulations with and without EMIC waves produce similar flux levels during the observed enhancement, the contribution of additional EMIC waves is not responsible for the lower flux value. As discussed above, the insufficient local acceleration during the October 2012 storm is a result of unusually low density. The same reason may explain the observed acceleration during June 2013, and will be a subject of further research.

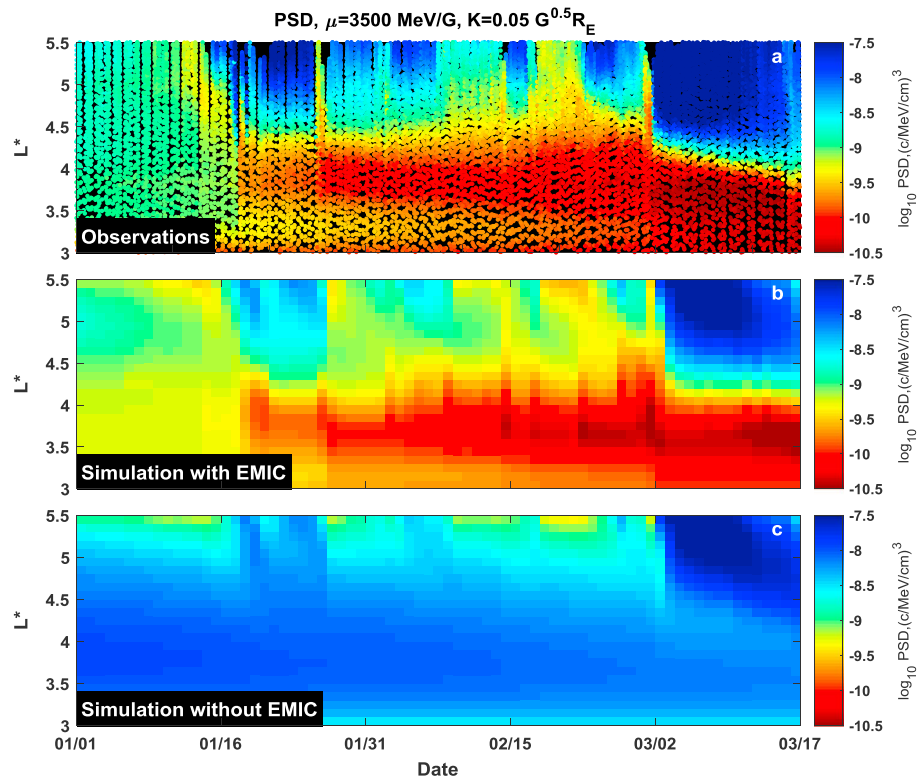


**Figure 4.** Evolution of the PSD from 1 January 2013 to 17 March 2013 for a fixed value of the first invariant,  $\mu = 3500$  MeV/G and  $K = 0.05 G^{1/2} R_E$  as a function  $L^*$ . The color bar is inverted to emphasize the deepening minimum of PSD. (a) Detailed Van Allen Probe observations, each point represents the 5 min average of the measurements. The black color is similar as on Figure 2. VERB code simulation results (a) with solar wind pressure parameterized EMIC waves and (c) without EMIC waves.

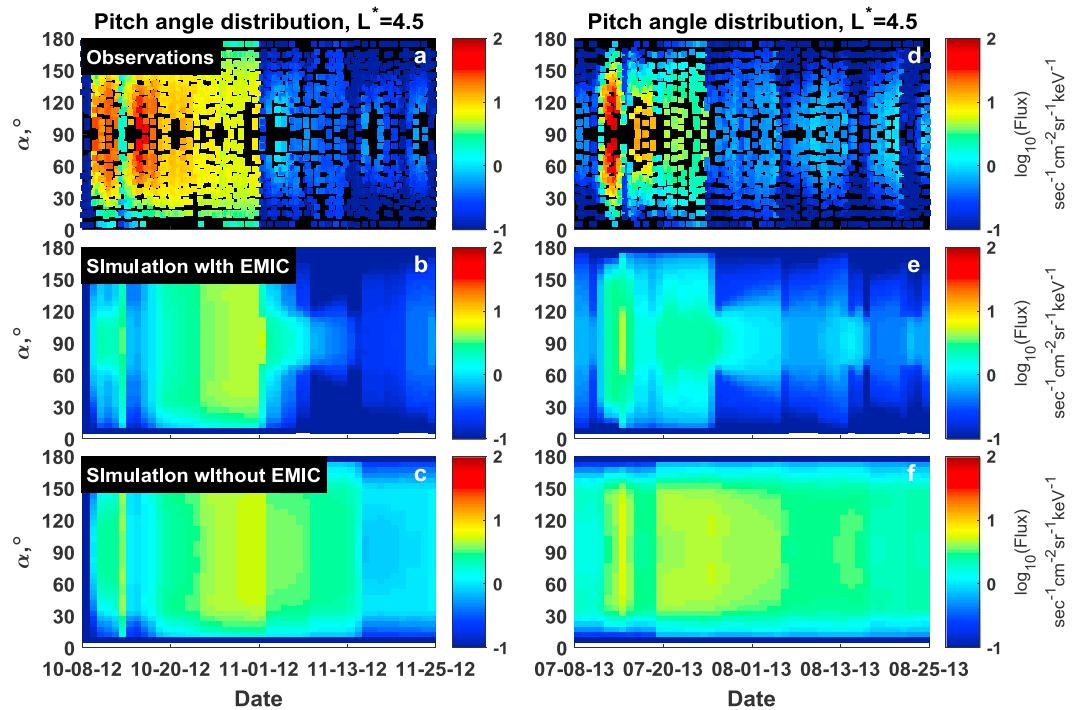


**Figure 5.** The pitch angle distribution evolution of 4.2 MeV electron fluxes at  $L^* = 4.5$  for the period of time: (a–c) from 8 October 2012 to 25 November 2012 and (d–f) from 8 July 2013 to 25 August 2013. Detailed REPT observations,  $L^* = 4.5 \pm 0.025$ , each point represents the 5-minute average of the measurements (Figures 5a and 5d). The black color is similar as on Figure 2 and it shows around  $90^\circ$  the absence of the equatorial measurements. VERB code simulation results with solar wind pressure parameterized EMIC waves (Figures 5b and 5e); VERB code simulation results without EMIC waves (Figures 5c and 5f). Similar to Figure 2, the vertical description on the left side of each row of panels indicates the observations, the simulation with and without EMIC waves.

### 5. Conclusions

We performed multiple long-term VERB code simulations including different parameterizations of EMIC wave presence and EMIC wave intensity. The comparison of the observations with the simulation results showed that the addition of EMIC waves improves the modeled ultrarelativistic electron flux in comparison to simulations without EMIC waves. We found that the solar wind dynamic pressure provides better parameterization of the EMIC wave presence in comparison to  $Kp$  index,  $Dst$  index,  $AE$  index, and solar wind speed, and the best results were obtained by including EMIC waves when solar wind dynamic pressure was larger than or equal to 3 nPa.

We examined the simulations with different EMIC waves  $B_w^2$  and found that the best agreement is achieved at  $0.4 \text{ nT}^2$ . However, the EMIC wave diffusion coefficients include other factors such as MLT distribution and occurrence rate. Those factors were determined statistically during active geomagnetic conditions ( $AE \geq 300 \text{ nT}$ ). Since in this work we used various parameterizations to define the presence of the EMIC waves, the realistic values of MLT distribution and occurrence rate can be different. Re-evaluation of these factors may change EMIC wave  $B_w^2$ .

Eventually, we conducted the detailed comparison of observations with the simulation with  $0.4 \text{ nT}^2$  EMIC waves that were included when the solar wind dynamic pressure was larger than or equal to 3 nPa. We showed that the simulation reproduces the dynamics of the electron flux evolution. The difference in the magnitude of the modeled and observed fluxes may be due to the inaccuracy of the plasma density models that were used to calculate diffusion coefficients of chorus and hiss waves. However, the calculated example of the decay times showed good agreement, and the observed PSD local minimum in January and February 2013 was remarkably reproduced by the simulations. The comparison of the pitch angle distribution showed a clear narrowed signature of EMIC waves in the observations and in the simulation results. All those facts indicate that EMIC waves certainly provide the additional necessary loss mechanism and play an important role in ultrarelativistic electron population.

The found discrepancy between the simulation with EMIC waves and the observations can be connected to several reasons. The EMIC wave diffusion coefficients were calculated assuming the constant spectrum. However, the observations show that the EMIC wave spectrum may vary during different events [e.g., Meredith et al., 2014]. The upper frequency cutoff can be larger than its statistical value leading to the lower minimum resonant energy [Ukhorskiy et al., 2010]. In addition, the minimum resonant pitch angle and overall efficiency of the EMIC wave scattering can change with variation of the spectral characteristics, ion composition, and plasma density. The accurate representation of the EMIC wave spectrum can provide more accurate modeling of the pitch angle distribution and will be a subject of future studies.

**Appendix A: Simulations With Different Parameters of EMIC Wave Presence**

Figure A1 shows MAE for the simulations with different parameters of EMIC wave presence (see Table 1) and with different EMIC wave  $B_w^2$ . Each panel is similar to Figure 1 and represents a single parameter from Table 1.

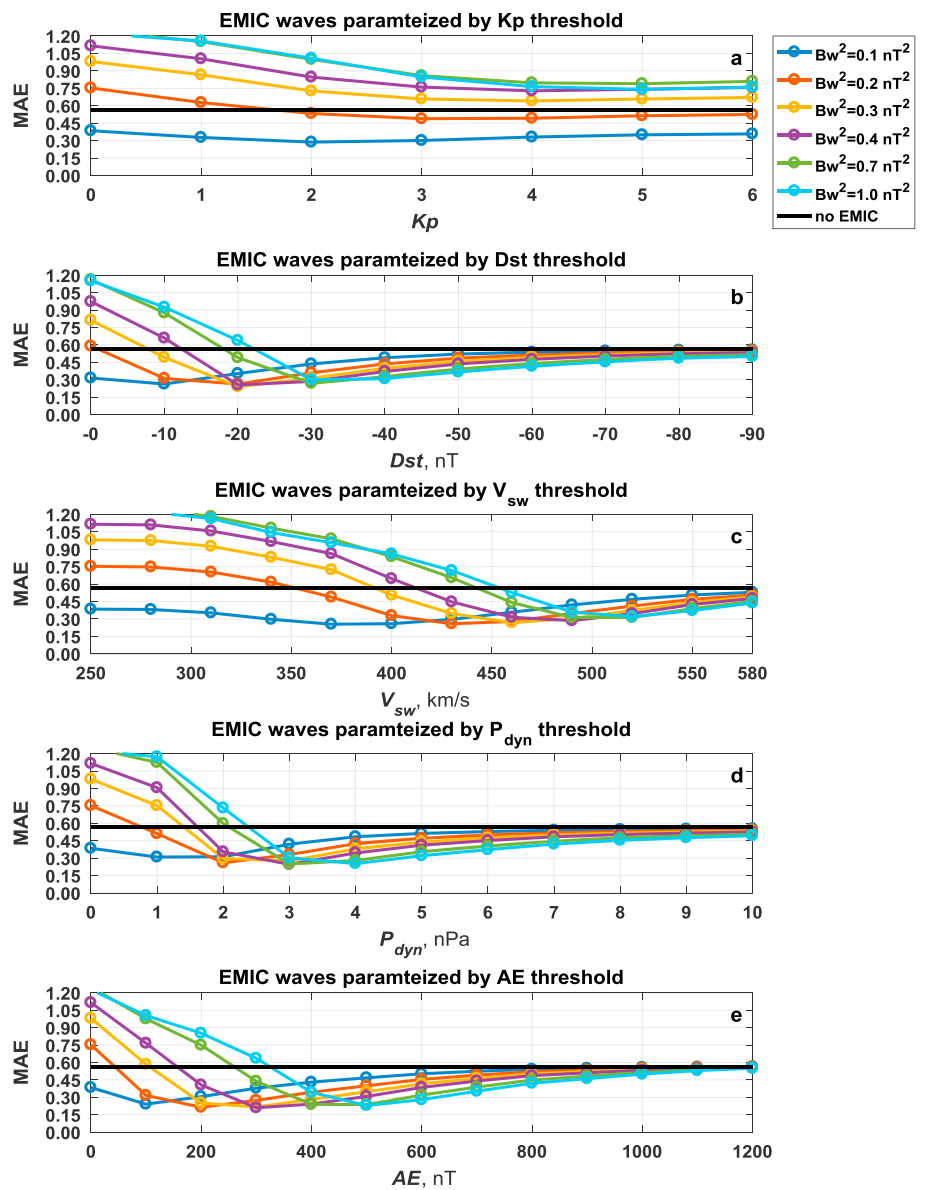


**Figure A1.** Dependence of the MAE for simulations with different parameterizations of EMIC waves. The color lines show the simulations with different EMIC waves  $B_w^2$ . The black line shows the simulation without EMIC waves. Parameterizations by (a) Kp index, (b) Dst index, (c) solar wind speed, (d) solar wind pressure, and (e) AE index.

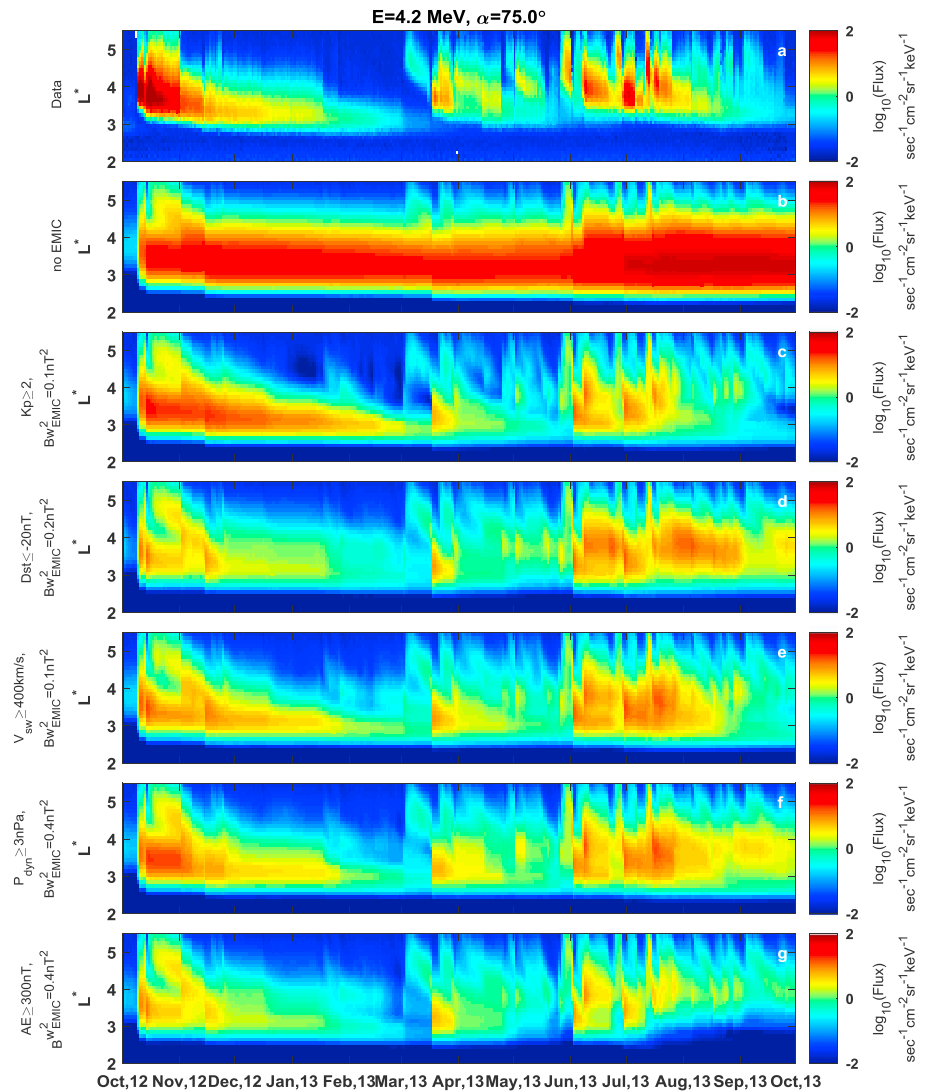


**Figure A2.** Evolution of the 4.2 MeV electron fluxes at the pitch angle of 75° as a function of time and  $L^*$ . The time period is the same as in Figure 2. (a) Daily binned REPT observations, on the simulation grid; (b) simulations without EMIC waves; and simulations with different EMIC wave parameterizations: parameterizations by (c)  $Kp$  index, (d)  $Dst$  index, (e) solar wind speed, (f) solar wind pressure, and (g)  $AE$  index.

Each panel shows that the similar low MAE can be achieved in different simulations (see section 4 for details). The low MAE values from different panels are comparable, which does not allow for giving preference to the single parameter from Table 1. To investigate which simulation provides better agreement with observations, we select five simulations for each EMIC wave presence parameter that corresponded to the lowest MAE values. The comparison of the modeled flux profiles and modeled pitch angle distribution with observations is described in detail in the supporting information.

The comparison between simulations with lowest MAE values and the same parameter of EMIC wave presence shows that the simulation results are close to each other. To investigate which parameter controlling the EMIC wave presence provides the best simulation results, we select the simulations with minimal MAE (see supporting information for details). Figure A2 is similar to Figure 2 and shows the evolution of the electron flux from observations, the simulation without EMIC waves and selected simulations with EMIC waves that correspond to minimal MAE. The observations on Figure A2 (and in the supporting information) are daily binned on the simulation grid for clarity. In general, each simulation with EMIC waves provides better agreement with data than the simulation without EMIC waves. The simulations with  $P_{dyn}$  and  $Kp$  provide better

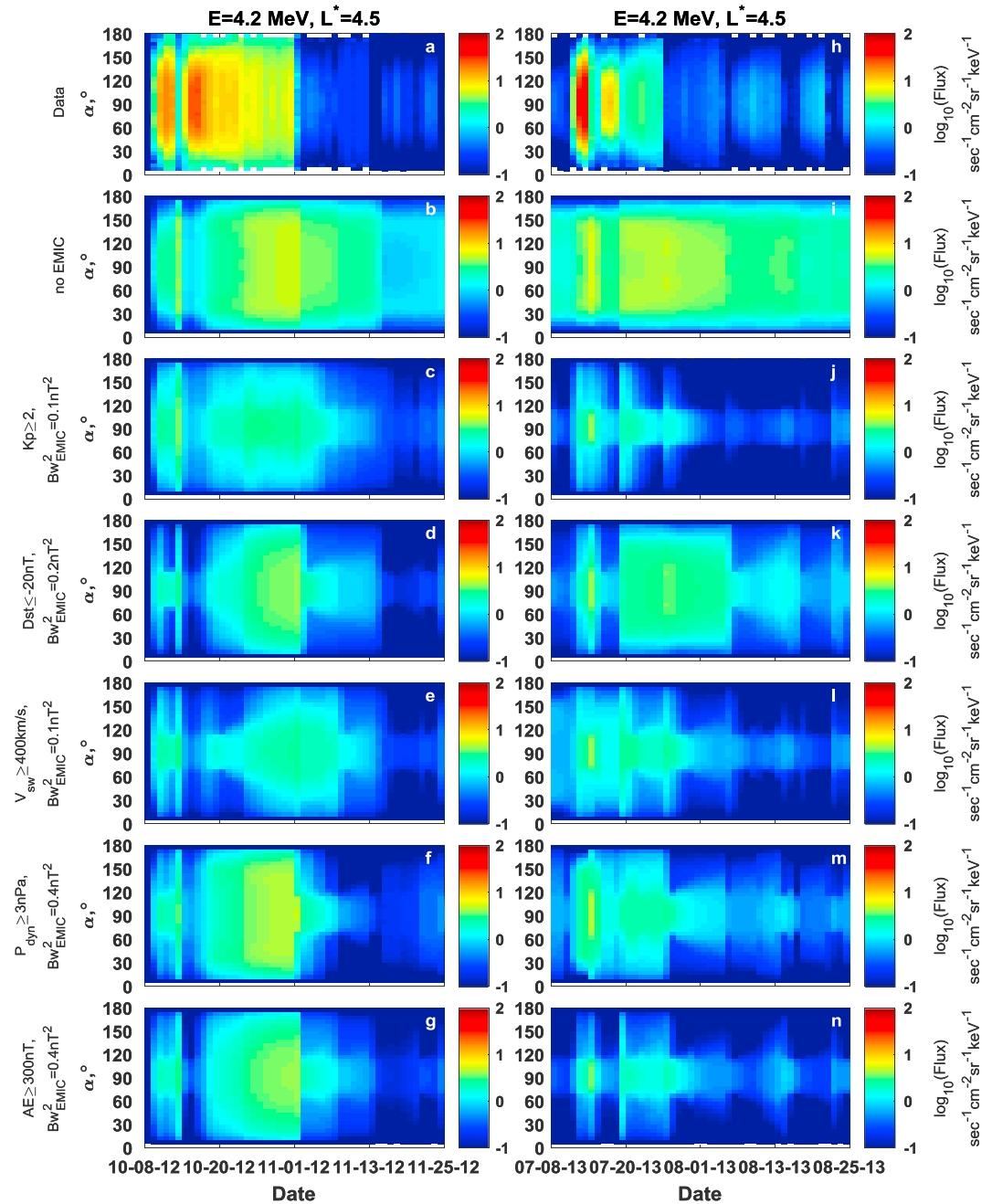


**Figure A3.** The pitch angle distribution evolution of 4.2 MeV electron fluxes at  $L^*=4.5$ . The time periods is the same as Figure 5. (a, h) Daily binned REPT observations, on the simulation grid; (b, i) simulations without EMIC waves; simulations with different EMIC wave parameterizations: parameterizations by (c, j)  $Kp$  index, (d, k)  $Dst$  index, (e, l) solar wind speed, (f, m) solar wind pressure, and (g, n)  $AE$  index.

dynamics of electron flux decay after the 8 October 2012 storm. All simulations with EMIC waves provide reasonable agreement for several weeks before and about 2 months after the storm on 17 March 2013. All simulations with EMIC waves provide better agreement with the observations in June 2013 and after, in comparison to the simulations without EMIC waves. Hence, all parameters from Table 1 provide the simulations with reasonable agreement with the measurements; however,  $P_{dyn}$  and  $Kp$  index are preferable.

To continue the investigation, we compare the pitch angle distribution during two periods with pronounced electron flux rapid depletion. Figure A3 is similar to Figure 5 and shows observed narrowing of pitch angle

distribution, which can be a signature of interaction with EMIC waves. Similar to Figure A2, the observations are daily binned on the simulation grid for clarity. The absence of the equatorial measurements is compensated by nearest point extrapolation. During the first period (from 8 October to 25 November 2012), the simulations with  $Dst$ ,  $P_{dyn}$ , and  $AE$  parameterization of EMIC wave presence reproduce the similar rapid depletion and provide similar pitch angle distribution after the dropout. During the second period (from 8 June to 25 July 2013), the simulations with  $V_{sw}$ ,  $P_{dyn}$ , and  $AE$  parameterization of EMIC wave presence reproduce the similar rapid depletion and provide similar narrow pitch angle distribution after the dropout. However, parameterization by  $P_{dyn}$  provide the best agreement with observations. As the result of considered comparison, we conclude that EMIC wave presence parameterized by  $P_{dyn}$  provides the best simulation results in comparison to the simulations with other parameters.

### Acknowledgments

The authors used geomagnetic indices provided by OMNIWeb (<http://omniweb.gsfc.nasa.gov/form/dx1.html>) and are grateful to the RBSP-ECT team for the provision of the Van Allen Probes observations (<http://www.rbsp-ect.lanl.gov/>). The diffusion coefficients used in the VERB code are available on the Space Environment Modeling Group website (<ftp://rbm.epss.ucla.edu/>). The authors would like to acknowledge high-performance computing support from Yellowstone (ark:/85065/d7wd3xhc) provided by UCAR's Computational and Information System Laboratory, sponsored by the National Science Foundation and other agencies and computational and storage services associated with the Hoffman2 Shared Cluster provided by UCLA Institute for Digital Research and Education's Research Technology Group. This research was supported by the NASA grant NNX16AF91G and by European Union's Horizon 2020 research and innovation program under grant agreement 637302.

### References

- Baker, D. N., R. D. Belian, P. R. Higbie, R. W. Klebesadel, and J. B. Blake (1987), Deep dielectric charging effects due to high-energy electrons in Earth's outer magnetosphere, *J. Electrostat.*, *20*(1), 3–19, doi:10.1016/0304-3886(87)90082-9.
- Baker, D. N., et al. (2013a), A long-lived relativistic electron storage ring embedded in Earth's outer Van Allen belt, *Science*, *340*(6129), 186–190, doi:10.1126/science.1233518.
- Baker, D. N., et al. (2013b), The Relativistic Electron-Proton Telescope (REPT) instrument on board the Radiation Belt Storm Probes (RBSP) spacecraft: Characterization of Earth's radiation belt high-energy particle populations, *Space Sci. Rev.*, *179*(1–4), 337–381, doi:10.1007/s11214-012-9950-9.
- Blake, J. B., et al. (2013), The Magnetic Electron Ion Spectrometer (MagEIS) instruments aboard the Radiation Belt Storm Probes (RBSP) spacecraft, *Space Sci. Rev.*, *179*(1–4), 383–421, doi:10.1007/s11214-013-9991-8.
- Blum, L. W., O. Agapitov, J. W. Bonnell, C. Kletzing, and J. Wygant (2016), EMIC wave spatial and coherence scales as determined from multipoint Van Allen Probe measurements, *Geophys. Res. Lett.*, *43*, 4799–4807, doi:10.1002/2016GL068799.
- Brautigam, D. H., and J. M. Albert (2000), Radial diffusion analysis of outer radiation belt electrons during the October 9, 1990, magnetic storm, *J. Geophys. Res.*, *105*(A1), 291–309, doi:10.1029/1999JA900344.
- Carpenter, D. L., and R. R. Anderson (1992), An ISEE/whistler model of equatorial electron density in the magnetosphere, *J. Geophys. Res.*, *97*(A2), 1097–1108, doi:10.1029/91JA01548.
- Drozdo, A. Y., Y. Y. Shprits, K. G. Orlova, A. C. Kellerman, D. A. Subbotin, D. N. Baker, H. E. Spence, and G. D. Reeves (2015), Energetic, relativistic, and ultrarelativistic electrons: Comparison of long-term VERB code simulations with Van Allen Probes measurements, *J. Geophys. Res. Space Physics*, *120*, 3574–3587, doi:10.1002/2014JA020637.
- Drozdo, A. Y., Y. Y. Shprits, N. A. Aseev, A. C. Kellerman, and G. D. Reeves (2017), Dependence of radiation belt simulations to assumed radial diffusion rates tested for two empirical models of radial transport, *Space Weather*, *15*, 150–162, doi:10.1002/2016SW001426.
- Engebretson, M. J., et al. (2015), Van Allen probes, NOAA, GOES, and ground observations of an intense EMIC wave event extending over 12 h in magnetic local time, *J. Geophys. Res. Space Physics*, *120*, 5465–5488, doi:10.1002/2015JA021227.
- Fraser, B. J., and T. S. Nguyen (2001), Is the plasmapause a preferred source region of electromagnetic ion cyclotron waves in the magnetosphere?, *J. Atmos. Sol. Terr. Phys.*, *63*(11), 1225–1247, doi:10.1016/S1364-6826(00)00225-X.
- Funsten, H. O., et al. (2013), Helium, Oxygen, Proton, and Electron (HOPE) mass spectrometer for the Radiation Belt Storm Probes mission, *Space Sci. Rev.*, *179*(1–4), 423–484, doi:10.1007/s11214-013-9968-7.
- Glauert, S. A., R. B. Horne, and N. P. Meredith (2014), Three-dimensional electron radiation belt simulations using the BAS Radiation Belt model with new diffusion models for chorus, plasmaspheric hiss, and lightning-generated whistlers, *J. Geophys. Res. Space Physics*, *119*, 268–289, doi:10.1002/2013JA019281.
- Halford, A. J., B. J. Fraser, and S. K. Morley (2010), EMIC wave activity during geomagnetic storm and non-storm periods: CRRES results, *J. Geophys. Res.*, *115*, A12248, doi:10.1029/2010JA015716.
- Halford, A. J., B. J. Fraser, S. K. Morley, S. R. Elkington, and A. A. Chan (2016), Dependence of EMIC wave parameters during quiet, geomagnetic storm, and geomagnetic storm phase times, *J. Geophys. Res. Space Physics*, *121*, 6277–6291, doi:10.1002/2016JA022694.
- Horne, R. B., and R. M. Thorne (1998), Potential waves for relativistic electron scattering and stochastic acceleration during magnetic storms, *Geophys. Res. Lett.*, *25*(15), 3011–3014, doi:10.1029/98GL01002.
- Horne, R. B., N. P. Meredith, R. M. Thorne, D. Heynderickx, R. H. A. Iles, and R. R. Anderson (2003), Evolution of energetic electron pitch angle distributions during storm time electron acceleration to megaelectronvolt energies, *J. Geophys. Res.*, *108*(A1), 1016, doi:10.1029/2001JA009165.
- Kersten, T., R. B. Horne, S. A. Glauert, N. P. Meredith, B. J. Fraser, and R. S. Grew (2014), Electron losses from the radiation belts caused by EMIC waves, *J. Geophys. Res. Space Physics*, *119*, 8820–8837, doi:10.1002/2014JA020366.
- Kim, K.-C., and Y. Shprits (2013), Long-term relativistic radiation belt electron responses to GEM magnetic storms, *J. Atmos. Sol. Terr. Phys.*, *100–101*, 59–67, doi:10.1016/j.jastp.2013.04.007.
- Kim, K.-C., Y. Shprits, D. Subbotin, and B. Ni (2011), Understanding the dynamic evolution of the relativistic electron slot region including radial and pitch angle diffusion, *J. Geophys. Res.*, *116*, A10214, doi:10.1029/2011JA016684.
- Kim, K.-C., Y. Shprits, D. Subbotin, and B. Ni (2012), Relativistic radiation belt electron responses to GEM magnetic storms: Comparison of CRRES observations with 3-D VERB simulations, *J. Geophys. Res.*, *117*, A08221, doi:10.1029/2011JA017460.
- Li, W., Y. Y. Shprits, and R. M. Thorne (2007), Dynamic evolution of energetic outer zone electrons due to wave-particle interactions during storms, *J. Geophys. Res.*, *112*, A10220, doi:10.1029/2007JA012368.
- Lyons, L. R., and R. M. Thorne (1972), Parasitic pitch angle diffusion of radiation belt particles by ion cyclotron waves, *J. Geophys. Res.*, *77*(28), 5608–5616, doi:10.1029/JA077i028p05608.
- Ma, Q., et al. (2015), Modeling inward diffusion and slow decay of energetic electrons in the Earth's outer radiation belt, *Geophys. Res. Lett.*, *42*, 987–995, doi:10.1002/2014GL029777.
- Mauk, B. H., N. J. Fox, S. G. Kanekal, R. L. Kessel, D. G. Sibeck, and A. Ukhorskiy (2013), Science objectives and rationale for the Radiation Belt Storm Probes mission, *Space Sci. Rev.*, *179*(1–4), 3–27, doi:10.1007/s11214-012-9908-y.

- Meredith, N. P., R. M. Thorne, R. B. Horne, D. Summers, B. J. Fraser, and R. R. Anderson (2003), Statistical analysis of relativistic electron energies for cyclotron resonance with EMIC waves observed on CRRES, *J. Geophys. Res.*, *108*(A6), 1250, doi:10.1029/2002JA009700.
- Meredith, N. P., R. B. Horne, T. Kersten, B. J. Fraser, and R. S. Grew (2014), Global morphology and spectral properties of EMIC waves derived from CRRES observations, *J. Geophys. Res. Space Physics*, *119*, 5328–5342, doi:10.1002/2014JA020064.
- Ozeke, L. G., I. R. Mann, K. R. Murphy, I. Jonathan Rae, and D. K. Milling (2014), Analytic expressions for ULF wave radiation belt radial diffusion coefficients, *J. Geophys. Res. Space Physics*, *119*, 1587–1605, doi:10.1002/2013JA019204.
- Reeves, G. D., K. L. McAdams, R. H. W. Friedel, and T. P. O'Brien (2003), Acceleration and loss of relativistic electrons during geomagnetic storms, *Geophys. Res. Lett.*, *30*(10), 1529, doi:10.1029/2002GL016513.
- Roederer, J. G. (1970), *Dynamics of Geomagnetically Trapped Radiation*, Springer, Berlin.
- Schulz, M., and L. J. Lanzerotti (1974), *Particle Diffusion in the Radiation Belts, Physics and Chemistry in Space*, Springer, Berlin.
- Shprits, Y. Y., and B. Ni (2009), Dependence of the quasi-linear scattering rates on the wave normal distribution of chorus waves, *J. Geophys. Res.*, *114*, A11205, doi:10.1029/2009JA014223.
- Shprits, Y. Y., W. Li, and R. M. Thorne (2006), Controlling effect of the pitch angle scattering rates near the edge of the loss cone on electron lifetimes, *J. Geophys. Res.*, *111*, A12206, doi:10.1029/2006JA011758.
- Shprits, Y. Y., D. Subbotin, A. Drozdov, M. E. Usanova, A. Kellerman, K. Orlova, D. N. Baker, D. L. Turner, and K.-C. Kim (2013), Unusual stable trapping of the ultrarelativistic electrons in the Van Allen radiation belts, *Nat. Phys.*, *9*(11), 699–703, doi:10.1038/nphys2760.
- Shprits, Y. Y., et al. (2016), Wave-induced loss of ultra-relativistic electrons in the Van Allen radiation belts, *Nat. Commun.*, *7*, 12883, doi:10.1038/ncomms12883.
- Shprits, Y. Y., A. Kellerman, N. Aseev, A. Y. Drozdov, and I. Michaelis (2017), Multi-MeV electron loss in the heart of the radiation belts, *Geophys. Res. Lett.*, *44*, 1204–1209, doi:10.1002/2016GL072258.
- Shue, J.-H., et al. (1998), Magnetopause location under extreme solar wind conditions, *J. Geophys. Res.*, *103*(A8), 17,691–17,700, doi:10.1029/98JA01103.
- Spasojevic, M., Y. Y. Shprits, and K. Orlova (2015), Global empirical models of plasmaspheric hiss using Van Allen Probes, *J. Geophys. Res. Space Physics*, *120*, 10,370–10,383, doi:10.1002/2015JA021803.
- Subbotin, D. A., and Y. Y. Shprits (2009), Three-dimensional modeling of the radiation belts using the Versatile Electron Radiation Belt (VERB) code, *Space Weather*, *7*, S10001, doi:10.1029/2008SW000452.
- Subbotin, D. A., and Y. Y. Shprits (2012), Three-dimensional radiation belt simulations in terms of adiabatic invariants using a single numerical grid, *J. Geophys. Res.*, *117*, A05205, doi:10.1029/2011JA017467.
- Subbotin, D. A., Y. Y. Shprits, and B. Ni (2011), Long-term radiation belt simulation with the VERB 3-D code: Comparison with CRRES observations, *J. Geophys. Res.*, *116*, A12210, doi:10.1029/2011JA017019.
- Summers, D., and R. M. Thorne (2003), Relativistic electron pitch-angle scattering by electromagnetic ion cyclotron waves during geomagnetic storms, *J. Geophys. Res.*, *108*(A4), 1143, doi:10.1029/2002JA009489.
- Su, Z., F. Xiao, H. Zheng, and S. Wang (2011), CRRES observation and STEERB simulation of the 9 October 1990 electron radiation belt dropout event, *Geophys. Res. Lett.*, *38*, L06106, doi:10.1029/2011GL046873.
- Tetrick, S. S., et al. (2017), Location of intense electromagnetic ion cyclotron (EMIC) wave events relative to the plasmopause: Van Allen Probes observations, *J. Geophys. Res. Space Physics*, *122*, 4064–4088, doi:10.1002/2016JA023392.
- Thorne, R. M., et al. (2013a), Evolution and slow decay of an unusual narrow ring of relativistic electrons near  $L \sim 3.2$  following the September 2012 magnetic storm, *Geophys. Res. Lett.*, *40*, 3507–3511, doi:10.1002/grl.50627.
- Thorne, R. M., et al. (2013b), Rapid local acceleration of relativistic radiation-belt electrons by magnetospheric chorus, *Nature*, *504*(7480), 411–414, doi:10.1038/nature12889.
- Tsyganenko, N. A. (1989), A magnetospheric magnetic field model with a warped tail current sheet, *Planet. Space Sci.*, *37*(1), 5–20, doi:10.1016/0032-0633(89)90066-4.
- Tsyganenko, N. A., and M. I. Sitnov (2007), Magnetospheric configurations from a high-resolution data-based magnetic field model, *J. Geophys. Res.*, *112*, A06225, doi:10.1029/2007JA012260.
- Tu, W., G. S. Cunningham, Y. Chen, M. G. Henderson, E. Camporeale, and G. D. Reeves (2013), Modeling radiation belt electron dynamics during GEM challenge intervals with the DREAM3D diffusion model, *J. Geophys. Res. Space Physics*, *118*, 6197–6211, doi:10.1002/jgra.50560.
- Ukhorskiy, A. Y., Y. Y. Shprits, B. J. Anderson, K. Takahashi, and R. M. Thorne (2010), Rapid scattering of radiation belt electrons by storm-time EMIC waves, *Geophys. Res. Lett.*, *37*, L09101, doi:10.1029/2010GL042906.
- Usanova, M. E., I. R. Mann, I. J. Rae, Z. C. Kale, V. Angelopoulos, J. W. Bonnell, K.-H. Glassmeier, H. U. Auster, and H. J. Singer (2008), Multipoint observations of magnetospheric compression-related EMIC Pc1 waves by THEMIS and CARISMA, *Geophys. Res. Lett.*, *35*, L17S25, doi:10.1029/2008GL034458.
- Usanova, M. E., I. R. Mann, J. Bortnik, L. Shao, and V. Angelopoulos (2012), THEMIS observations of electromagnetic ion cyclotron wave occurrence: Dependence on AE, SYM-H, and solar wind dynamic pressure, *J. Geophys. Res.*, *117*, A10218, doi:10.1029/2012JA018049.
- Usanova, M. E., et al. (2014), Effect of EMIC waves on relativistic and ultrarelativistic electron populations: Ground-based and Van Allen Probes observations, *Geophys. Res. Lett.*, *41*, 1375–1381, doi:10.1002/2013GL059024.